A Minimal Colloid Model of Solution Crystallization Nucleates Crystals Classically

Journal:	*Soft Matter*
Manuscript ID	SM-ART-11-2023-001609.R1
Article Type:	Paper
Date Submitted by the Author:	08-Feb-2024
Complete List of Authors:	Chen, Gary; University of Houston Gallegos, Mariah; University of Houston Soetrisno, Diego; University of Houston Vekilov, Peter; University of Houston, Department of Chemistry Conrad, Jacinta; University of Houston,

Soft Matter

A Minimal Colloid Model of Solution Crystallization Nucleates Crystals Classically[†]

Gary Chen,[*a] Mariah J. Gallegos,[a] Diego D. Soetrisno,[a] Peter G. Vekilov,[a,b] and Jacinta C. Conrad[a]

A fundamental assumption of the classical theories of crystal nucleation is that the individual molecules from the "old" phase associate to an emerging nucleus individually and sequentially. Numerous recent studies of crystal nucleation in solution have revealed nonclassical pathways, whereby crystal nuclei are hosted and fed by amorphous clusters pre-formed in the solution. A sizable knowledge gap has persisted, however, in the definition of the molecular-level parameters that direct a solute towards classical or nonclassical nucleation. Here we construct a suspension of colloid particles of hydrodynamic diameter 1.1 μm and monitor their individual motions towards a quasi-two-dimensional crystal by scanning confocal microscopy. We combine electrostatic repulsion and polymer-induced attraction to obtain a simple isotropic pair interaction potential with a single attractive minimum of tunable depth between 1.2 $k_B T$ and 2.7 $k_B T$. We find that even the smallest aggregates that form in this system structure as hexagonal two-dimensional crystals and grow and maturate by the association and exchange of single particles from the solution, signature behaviors during classical nucleation. The particles in the suspension equilibrate with those in the clusters and the volume fractions of suspensions at equilibrium correspond to straightforward thermodynamic predictions based on depth of the interparticle attraction. These results demonstrate that classical nucleation is selected by particles interacting with a minimal potential and present a benchmark for future modifications of the molecular interactions that may induce nonclassical nucleation.

1 Introduction

Crystallization, the formation of translationally-symmetric arrays of atoms, molecules, or particles, is an essential part of the synthesis of geological, biological and engineered materials.[1,2] Crystallization divides into nucleation, in which the assembly of initial crystal domains is impeded by the free energy cost of the emerging crystal-solution interface, and growth, which does not encounter thermodynamic obstacles.[3–5] Classical theories of crystal nucleation and growth assume that the building constituents attach to a growing nucleus or crystal individually and sequentially.[6–12] In the last 20 or so years, experiments with diverse systems crystallizing in solution have exposed a role for precursors that may be liquid, amorphous, or even crystalline as nucleation hosts and crystal building blocks.[13–20] Nonclassical nucleation and growth have become so ubiquitous that rare instances of demonstrated classical behaviors are now celebrated.[21,22]

What has been missing from the discussion of classical and nonclassical crystal nucleation and growth pathways in solution is rationalization of the molecular-level parameters that direct a crystallizing system towards one of the two mechanisms. Attempting to address this issue, observations with calcite – a mineral found in rocks, shells, skeletons, and tissues[23] – were interpreted to suggest that the shift from classical to nonclassical behavior may be driven by the increasing dominance of nonspecific intermolecular attraction over specific, i.e., short-ranged and directional, interactions.[24,25] Here we address the characteristics of the intermolecular interaction potential that may select classical or nonclassical crystallization behaviors in solution. We focus on crystal nucleation, for which the transition from classical to nonclassical pathways may accelerate the nucleation rate by multiple orders

[a] William A. Brookshire Department of Chemical and Biomolecular Engineering, University of Houston, 4226 Martin Luther King Boulevard, Houston, Texas 77204-4004, United States. Fax: + 1 713-743-4323; Tel: +1 713-743-4300; E-mail: jc-conrad@uh.edu, vekilov@uh.edu

[b] Department of Chemistry, University of Houston, 3585 Cullen Boulevard, Houston, Texas 77204-5003, United States.

‡ Additional footnotes to the title and authors can be included e.g. 'Present address:' or 'These authors contributed equally to this work' as above using the symbols: ‡, §, and ¶. Please place the appropriate symbol next to the author's name and include a \footnotetext entry in the the correct place in the list.

of magnitude.

In situ monitoring of crystal nucleation with near molecular resolution has mostly relied on two methods: atomic force microscopy (AFM)[26] and liquid cell transmission electron microscope (TEM).[27] AFM (lateral resolution ∼30 nm, vertical resolution ∼0.1 nm, temporal resolution ∼min), however, is too slow to provide dynamics of individual constituents. Further, AFM only images objects adhering to a substrate,[28] which may impact the evolution of the nuclei.[28,29] More reliable is the use of the substrate as a trap for critical and near critical clusters formed in the solution,[26,30] but this imaging protocol is handicapped by the possibility of missing crucial stages in the nuclei evolution. Liquid phase TEM imaging (lateral resolution ∼0.2 nm, temporal resolution ∼0.1 fps) has been recently employed to examine the pathways for nucleation for individual nanoparticles[31] and assemblies of nanoparticles.[32–34] This technique is challenging to use, however, because it suffers from low signal-to-noise ratio[35,36] and effects of electron beam exposure.[37] An additional challenge of this modality is the extremely small imaged solution volume, of the order of a few femtoliters.[38] To increase the probability of a nucleation event in this small volume, high supersaturations, which may bias the nucleation pathway, are often employed. Finally, the interactions between small faceted nanoparticles are often directional and orientation-specific[39], making it difficult to deconvolve these interactions from those due to the interparticle potential.

To circumvent these challenges, we monitor the phase dynamics in a suspension of colloidal particles, as in numerous previous studies.[40–47] While interactions between micron-sized colloidal particles are much shorter-ranged (typically several percent of the particle diameter) than those of atomic or molecular systems (comparable to the atom/molecule size[48,49]), this model system is nonetheless able to reproduce many features of the phase behavior of atomic or molecular systems.[50,51] We employ fast-scanning confocal microscopy[52] (lateral spatial resolution ∼300 nm, temporal resolution ∼ 0.1s) and image processing algorithms[53] to track the motions of 1.1 μm diameter copolymer particles in dilute suspensions. The particle trajectories directly reveal the structures of the emerging clusters and their dynamics. An additional advantage of the chosen model is that we can engineer the interparticle interactions. We develop a minimal tunable isotropic interaction potential dominated by electrostatic repulsion and polymer-induced attraction.[54] We carefully balance these two forces to obtain a simple pair interaction potential, in which soft short-range repulsion transitions to attraction via a single minimum with adjustable depth. Electrostatic repulsion by the upper and lower cuvette walls confine the particles to motion in the image plane. We show that in this system, hexagonal two-dimensional crystals nucleate from solution and maturate following strictly classical pathways.

2 Materials and Methods

2.1 Particle synthesis

We synthesized poly (2,2,2-trifluoroethyl methacrylate-co-tert-butyl methacrylate) (TtMA) particles using an existing protocol.[55] The particles consist of a fluorescent core dyed with rho-

damine B methacrylate, a non-fluorescent shell sterically stabilized with poly(vinylpyrrolidone) (PVP), and negatively charged co-polymer brushes. Particles were synthesized with a volumetric ratio of 26:74 of 2,2,2-trifluoroethyl methacrylate (TFEMA; Synquest Laboratories) to tert-butyl methacrylate (tBMA). The density (1.15 g cm^{-3}) and refractive index ($n = 1.45$) of the particles and solution were estimated from the ideal mixing rule and Lorentz-Lorenz equation, respectively. An initiator-monomer (inimer), 2-(2-bromoisobutyryloxy) ethyl acrylate, was synthesized and included in both the core and shell synthesis as a growth initiator for the outer layer of negatively charged copolymer brush. The charged copolymer brush was composed of dimethylacrylamide and 2-acrylamido-2-methyl-1-propanesulfonic acid and was grafted onto the particles by atom transfer radical polymerization (ATRP). After each synthesis step, the particles were collected and washed by centrifugation with methanol or de-ionized water at least five times. After final centrifugation, the particles were resuspended in DI water at a volume fraction $\phi = 0.4$. The resulting suspension was stored in a refrigerator.

2.2 Particle characterization

The hydrodynamic radii of the particles after each synthesis step were measured by dynamic light scattering (DLS; ALV-GmBH instrument). Light scattering data were acquired at five angles $\theta = 60°, 75°, 90°, 105°,$ and $120°$. We obtained the normalized time autocorrelation function of the intensity of the scattering light $g^{(2)}(q, \tau)$ for a given delay time τ and wavevector $q = (4\pi n/\lambda)\sin(\theta/2)$, where $n = 1.333$ is the refractive index of water. Data were fit to a third-order cumulant model,[56]

$$g^{(2)}(q,\tau) = B + \beta \exp(-2\Gamma\tau)\left(1 + \frac{\mu_2}{2!}\tau^2 - \frac{\mu_3}{3!}\tau^3\right)^2 \quad (1)$$

where B is the baseline (≈ 1), $\beta \approx 1$ depends on the instrument geometry, $\Gamma = Dq^2$ is the intensity decay rate, τ is the delay time, μ_2 and μ_3 are the second and third moments of the mean, and D is the diffusion coefficient of the particles. From D, we determined the hydrodynamic radius of the particles, a, using the Stokes-Einstein relation,

$$D = \frac{k_B T}{6\pi\eta a}, \quad (2)$$

where η is the dynamic viscosity of the solvent (water).

The zeta potential $\zeta = -85 \pm 4$ mV of the particles was measured with a Nicomp 380 ZLS zeta sizer. For this measurement, the negatively charged particles were diluted in 10 mM Tris buffer ($\phi \approx 0.001$; pH = 7.5). Scanning electron microscopy (SEM, Axia ChemiSEM, ThermoFisher, Czech Republic) was applied to image the synthesized particles.

2.3 Sample preparation

Suspensions for imaging experiments were prepared by mixing stock suspensions of synthesized particles, deionized water, sodium hydroxide, and polyacrylamide (PAM, $M_w = 194$ kDa, $M_w/M_n = 1.25$, Polymer Source). Using capillary viscometry, we determine the polymer radius of gyration at infinite dilution as

$R_g = 22$ nm, leading to a size ratio $\xi = R_g/a = 0.04$. Samples at initial volume fraction $\phi_0 = 0.03$, 0.04, and 0.05 were mixed on a rolling mixer for at least 16 hours to ensure that they were homogenized. The final concentration of sodium hydroxide and PAM is given in the total sample volume.

Glass chambers were fabricated with glass cover slides and NOA 68T UV-curable epoxy (Norland Products Inc.). The glass slides (48×65 mm No. 1, Thermo, USA; 22×22 mm No. 1, VWR, Germany) were first immersed in a base bath (≈ 70 g L^{-1} KOH in isopropyl alcohol) for at least one hour and rinsed in deionized water. The glass slides were dried with nitrogen and then cleaned by low pressure air plasma (Harrick Plasma, USA) for at least 2 hours. A droplet (~ 2.2 μL) of the particle suspension was placed onto the cleaned glass slide and then covered by a cleaned cover slip. Capillary forces drove any occational bubbles to the edge of the cover slip, after which the chamber was sealed with epoxy.

2.4 Confocal imaging and analysis

Suspensions were imaged using a Leica SP8 microscope equipped with a 63x oil-immersion objective lens (numerical aperture of 1.4). At a given time point we acquired 3×3 image tile sets, in which each tile was 61.3 μm $\times$ 61.3 μm. To characterize the time evolution of the suspension, image tile sets were acquired every ten minutes for 16 to 28 hours. At least three replicates were taken for each sample . Particle trajectories were obtained using the Crocker and Grier algorithm in IDL.[53]

The ensemble-averaged 1D mean-square displacement $MSD = \langle (x(t+\tau) - x(t))^2 \rangle$ was calculated from the particle trajectories. We also evaluated the radial distribution function $g(r) = \frac{1}{2\pi r \rho N dr} \sum_{i=1}^{N} n_i(r)$, where $n_i(r)$ is the number of particles identified at distance between r and $r+dr$ away from a reference particle i, ρ is the mean particle number density, and N is the total number of identified particles. To characterize the local cluster structure, we calculated the 2D bond-orientational order parameter $\psi_6 = \frac{1}{n} \sum_{l=1}^{n} exp[i6\theta_l]$, where n is the number of nearest neighbor, θ_l is the angle between the vector connecting a nearest neighbor l and an arbitrary reference vector, and used its magnitude, $|\psi_6|$, as a metric for the closeness of the first neighbor shell to a hexagon (expected for a perfect 2D packing). We characterized the cluster size using the cluster radius of gyration $R_{g,c} = [(]\frac{1}{k} \sum_{i=1}^{k} (r_i - R_{CM})^2 + a^2]^{0.5}$, where k is number of particles in the cluster and r_i and R_{CM} are the positions of particle i in the cluster and the center of mass of the cluster, respectively. The Voronoi diagrams of clusters and their dual Delaunay triangulations were calculated from the particle centroid positions using standard MATLAB functions.

3 Results and Discussion

3.1 Characteristics of particles

The hydrodynamic diameter of the particles (Fig. 1a), determined from the scaling of the decay rate Γ of the light scattered by the particles with the wave vector q, is $2a = 1.1 \pm 0.1$ μm (Fig. 1b). The particles dispersed in DI water without salt or polymer form a quasi-2D layer in the thin sample chambers (Fig. 1c). The dynamics of the confined particles are diffusive, as indicated by the

linear scaling of the mean-square displacement (MSD) with time. Their diffusion coefficient, 0.116 μm^2 s^{-1}, is smaller than the free diffusivity $D_{S-E} = 0.143$ μm^2 s^{-1} predicted using the Stokes-Einstein equation and the hydrodynamic radius determined by light scattering in bulk samples. The smaller value may be due to interactions[57] between the particles and the glass substrate that impede diffusion.[58]
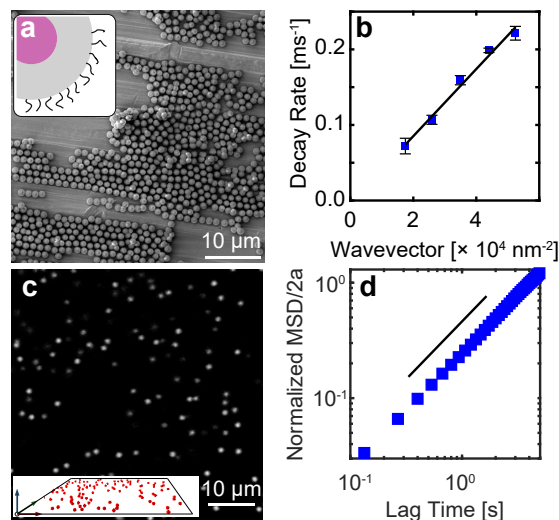

Fig. 1 Characterization of the particles. (a) SEM image of TtMA particles. Inset: illustration of particle composed of core, shell, and brush (not drawn to scale). (b) Decay rate of light scattering intensity as a function of wavevector. (c) Confocal micrograph of the particles suspension with initial volume fraction $\phi_0 = 0.05$ suspended in DI water. Inset: 3-D rendering of the particle positions, illustrating that the particles form a quasi-monolayer in the thin chamber. (d) Mean-square displacement (MSD) as a function of lag time of the TtMA particles suspended in DI water.

3.2 Interparticle potential

To tune the interactions between the TtMA particles, we add polyacrylamide (1.5 mg mL^{-1} = 0.3 c/c^*, where c^* is the overlap concentration), to induce depletion attraction, and NaOH, to partially screen the electrostatic repulsion. In the absence of added NaOH, particles appear well dispersed. The radial distribution function $g(r)$ is independent of time and increases from zero to one near $r = 2a$, where a is the hydrodynamic radius of the particles (Fig. 2a). This result suggests that the electrostatic repulsion due to the particle charge approximately cancels the depletion attraction caused by the added PAM; thus, the particles are slightly charged.

In samples with added NaOH, by contrast, confocal micrographs reveal clusters of particles (Fig. S1). The depletion attraction is sufficiently strong to overcome the partially-screened electrostatic repulsion, leading to aggregates of particles that evolve over time. The corresponding pair correlation functions exhibit local maxima and $g(r)$ varies with time (Fig. 2b-d). We obtain the interparticle potential $U(r)$ from $g(r)$ via $g(r) = \exp(-U(r)/k_BT)$.[59] The potential well depth U_0, determined as

the local minimum, is a function of the salt concentration for the range investigated here (10 – 50 mM). For [NaOH] = 10 mM, the well depth ($U_0 = 1.2\ k_BT$) is comparable to the thermal fluctuations (Fig. 2b) and particles are relatively well dispersed. For salt concentrations of 30 and 50 mM, the potential well depths are 1.7 and 2.7 k_BT, respectively. The pair correlation functions for these suspensions exhibit additional peaks in $g(r)$ (Fig. 2c,d)), consistent with structural correlations at distances greater the nearest-neighbor separation arising from larger clusters. We model the combined potential $U = U_{AO} + U_Y$ of our samples at various salt concentrations as the sum of the the the Asakura-Oosawa potential[60] and the Yukawa potential[61,62], which respectively describe the depletion attraction and electrostatic repulsion. The Asakura-Oosawa potential is given by $\frac{U_{AO}(r)}{k_BT} = -(\frac{3}{2})\phi_p\beta x^2$, where k_B is Boltzmann's constant, T is the temperature, r is the interparticle distance, β is the size ratio between the particle and the polymer, ϕ_p is the volume concentration of the polymer, and $x = (D + d - r)/d$ is a function of the particle diameter $D = 2a$ and polymer size $d = 2R_g$ (Fig. S3). The Yukawa potential is $U_Y(r) = \varepsilon \frac{\exp[-\kappa D(r/D-1)]}{r/D}$, where ε is the contact potential, and κ^{-1} is the Debye screening length. The potential well depth calculated from the model, $U_0 = -1.55 k_BT$, is in good agreement with the well depths evaluated from the experimentally determined $g(r)$ values.
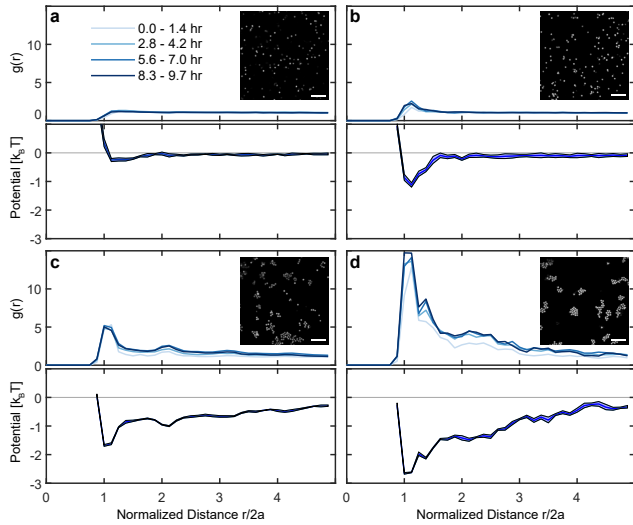

Fig. 2 Time evolution of the interparticle potential. Pair correlation function $g(r)$ (top) and the corresponding interparticle potential $U(k_BT)$ (bottom) over the times shown in (a) as functions of the normalized distance $r/2a$ between the centers of mass of two particles. The PAM concentration is 0.3 c/c^* and the NaOH concentrations are (a) 0, (b) 10, (c) 30, and (d) 50 mM. The shaded region in the potential plots indicates the error in the interparticle potential, calculated as the standard deviation of three measurements on one sample after equilibrium is reached. Insets: representative micrographs of particles at equilibrium at different NaOH concentrations. The scale bar equals 10 μm.

3.3 Cluster characterization

To characterize clusters of particles, we first identify the nearest neighbors using a cutoff distance of $2.5a$, determined from the first local minimum of $g(r)$, and assign particles to clusters based on neighbor connectivity (Fig. 3). For a representative sample with $\phi_0 = 0.03$ at [PAM]=$0.3c/c^*$ and 30 mM NaOH, the cluster size distribution evolves over time (Fig. 3(b)). On time scales of 8 h the cluster number density reaches a steady state, and exhibits a weak shoulder at $\sim$ 10 particles per cluster (inset of Fig. 3(b)). The presence of this weak second local maximum is similar to that found in simulations of the cluster size distribution for particles with competing attractive and repulsive interactions (a combined Lennard-Jones and Yukawa potential).[63]

3.4 Equilibrium between particles and clusters

To monitor the approach of the particle suspension to equilibrium with the crystals, we examined the evolution of the volume fraction of monomeric particles ϕ_m. We find that ϕ_m decreases over time as particles are incorporated into clusters (Fig. 3(c)). At long times, $\phi_m(t)$ reaches a steady value ϕ_e. Two observations identify ϕ_e as the particle solubility, i.e., the volume fraction at which the particles are in equilibrium with the clusters.[64] First, during the time that ϕ_m is steady, the clusters exchange particles with the solution. The steady ϕ_m indicates that during any length of time, the numbers of monomeric particles that dissociate from or associate to clusters are equal. Second, ϕ_e is independent of the initial particle volume fraction.

The solubility ϕ_e depends on the salt concentration in the solution (Fig. 3(d)) because the NaOH concentration affects the interparticle interactions (Fig. 2). Notably, ϕ_e is a non-monotonic function of salt concentration (Fig. 3(d)), first decreasing and then increasing with increasing [NaOH]. These behaviors are similar to observations in proteins and colloids, where the decreasing-ϕ_e regime is referred to as salting-out and the increasing-ϕ_e regime as salting-in.[65] Salting-out has been attributed to the screening of the electrostatic interactions between the particles in the suspension by the ions[66] (also seen in Fig. 2). Salting-in has been tentatively assigned to association of ions to the particle surface (in our case, likely, to the charged amide and sulfonic groups of the polymer brushes on the particle surfaces), which lowers their charge, attenuates their repulsion, and allows greater volume fraction in the solution.[67]

We relate ϕ_e to the strength of the interparticle interactions. We denote as ψ the energy of the bond between two particles in a cluster, which corresponds to the minima in the interparticle interaction potentials in Fig. 2. The enthalpy Δh to transfer a particle from the suspension to a cluster, equal to the enthalpy of cluster formation per particle, is then $\Delta h = z\psi/2$, where $z = 6$ is the number of nearest neighbors of a particle in a two-dimensional cluster. With the entropy change of cluster formation $\Delta s = k\ln\phi$ per particle, the difference of the chemical potential of a particle in the suspension and in a cluster is $\Delta\mu = \Delta h - T\Delta s = z\psi/2 - k_BT\ln\phi$. At equilibrium $\Delta\mu = 0$, and we obtain for the solubility $\ln\phi_e = z\psi/2k_BT$. Using $\phi_e = 0.017$ and 0.004 for, respectively, 10 and 30 mM NaOH (Fig. 3(d)), we obtain $\psi = -1.2\ k_BT$ and $-1.7\ k_BT$, in good agreement with the minima in $U(r)$ (Fig. 2(b) and (c)). At 50 mM NaOH, however, the $U(r)$ minimum (Fig. 2(d)) suggests $\psi \approx -2.7 k_BT$, which would

predict $\phi_e \approx 0.00022$. The actual solubility, $\phi_e \approx 0.015$, is substantially higher. This discrepancy suggests that at high concentrations NaOH may induce a more elaborate interplay between enthalpic, entropic, and spatial interactions involving the polymer brushes on the particles and the polyacrylamide present in the suspension. We posit that the effects of NaOH on the behaviors of particles in the suspension diverge from its effects on the particles in the clusters. Hence, the solubility, which is a property of the equilibrium between the suspension and the clusters, responds differently to high NaOH concentration than the cluster structure, used to evaluate $U(r)$.
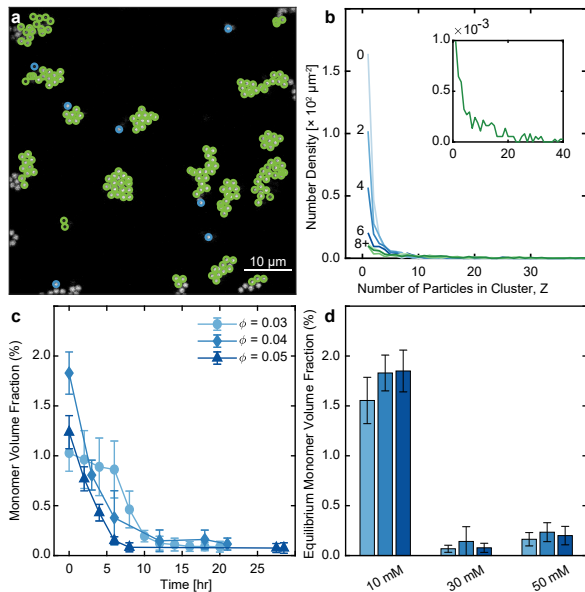

Fig. 3 Characterization of the clusters of particles. (a) Confocal micrograph of clusters of particles. A cutoff of $2.5a$ is used to identify neighboring particles. Cluster and isolated particles are shaded blue and green, respectively. (b) Cluster size distributions at the times indicated by the number next to each curve, in hours, for a suspension with $\phi_0 = 0.03$, [PAM]= 0.3 c/c^*, and [NaOH] = 30 mM. The inset to (b)zooms on the data at 8h. (c, d) Determination of the volume fraction ϕ_e at which particles are in equilibrium with the clusters. (c) Evolution of the monomer volume fraction ϕ_m at three initial particle volume fractions ϕ_0 for [NaOH] = 10 mM. (d) The equilibrium ϕ_e, evaluated as the mean of the ϕ_m values measured after steady state is reached, for [NaOH] = 10, 30, and 50 mM. The three bars indicate three distinct initial monomer volume fractions ϕ_0 as in (c). Error bars indicate one standard deviation from the mean.

3.5 Structural measurements indicate that clusters nucleate classically

The structure of clusters changes over time due to addition and rearrangement of particles. We characterize this structural evolution in three ways. First, we construct the Voronoi tessellation for particles in clusters of different ages (shown for a representative cluster in Fig. 4a). For a close-packed 2-D lattice, the area fractions occupied by the center particle in the polygons created by the Voronoi tesselation and the Delaunay triangulation are $\phi_{\text{hex,V}} = \sqrt{3}\pi/6 \approx 0.907$ and $\phi_{\text{hex,D}} = \sqrt{3}\pi/18 \approx 0.302$, respectively, with $\phi_{\text{hex,D}}/\phi_{\text{hex,V}} = 1/3$. For the representative clus-

ter from a suspension with $0.3c/c^*$ and 30 mM NaOH shown in Fig. 4a, $\phi_{\text{hex,V}} = 0.58 \pm 0.03$ and $\phi_{\text{hex,D}} = 0.20 \pm 0.01$, respectively, for the Voronoi tessellation and Delaunay triangulation, and $\phi_{\text{hex,D}}/\phi_{\text{hex,V}} = 0.34 \pm 0.02$. The similarity of the experimentally measured $\phi_{\text{hex,D}}/\phi_{\text{hex,V}}$ to the theoretical prediction suggests that the clusters are close-packed, with an effective particle size ($\sim 1.5\,\mu$m) that is somewhat larger than the hydrodynamic diameter ($1.1\,\mu$m).

Second, we evaluate the average bond orientational order parameter $\overline{\psi_6}$, averaged over all the particles in a cluster.[68] For the representative cluster shown in Fig. 4a, both the number of particles and $\overline{\psi_6}$ fluctuate over time. The temporal fluctuations in $\overline{\psi_6}$ correlate to changes in the number of particles in the cluster as particles join or leave (Fig. 4(b)).

Third, we calculate the structural order parameter $\langle\psi_6\rangle$ averaged over all clusters in a sample at various time points during the cluster evolution. Although the cluster number density distribution changes over time (Fig. 3b), $\langle\psi_6\rangle \sim 0.7$ is, within the data uncertainty, independent of time and ϕ_0 (Fig. 4c). These three data sets reveal that all observed clusters, independent of their size, age, initial volume fraction, or time of formation, structure as hexagonal two-dimensional crystals. No disordered clusters, which may host the nucleation of hexagonal crystalline clusters if nucleation were nonclassical, are observed. These observations are consistent with the tenets of classical nucleation theory, which posit that even the smallest domains of a new phase structure as macroscopic crystals, and are incompatible with nonclassical mechanisms of crystal nucleation, in which crystal nuclei are hosted by distinctly structured precursors. We posit that crystals in this system nucleate classically because the interparticle potential contains only a single minimum, and there is no secondary minimum to stabilize the precursors.

3.6 Clusters mature via Ostwald ripening

Observation with all tested initial volume fractions ϕ_0 of particles reveal that the total number of clusters increases during the initial $\sim$3.5h after supersaturation is imposed and decreases at longer times (Fig. 5a). The initial increase of the cluster number indicates that new clusters continue to nucleate during the first 3.5h. Accordingly, greater ϕ_0, i.e. a higher supersaturation, results in more clusters at all times owing to faster nucleation rate. Both the average (Fig. 5(b)) and maximum (Fig. 5(c)) cluster sizes grow with time for the three ϕ_0 examined. Notably, the maximum size reached by the cluster population decreases as the initial volume fraction increases. The width of the cluster size distribution also grows with time, indicating a broader range of cluster sizes (Fig. 5(d)). The observed trends of the cluster sizes and size distributions arise from different sensitivity of the rates of nucleation and growth to the supersaturation $\Delta\phi = \phi_m - \phi_e$. The nucleation rate B increases as a power law with $\Delta\phi$, i.e., $B = k_b\Delta\phi^b$, where k_b is a nucleation constant, and typically $5 \leq b \leq 10$. The cluster growth rate G, however, is a weaker function of $\Delta\phi$, $G = k_g\Delta\phi^g$, where k_g is a growth constant and typically $1 \leq g \leq 2$.[69] Owing to its stronger sensitivity to supersaturation, crystal nucleation dominates crystal growth at higher supersaturations (i.e., larger ϕ_0),
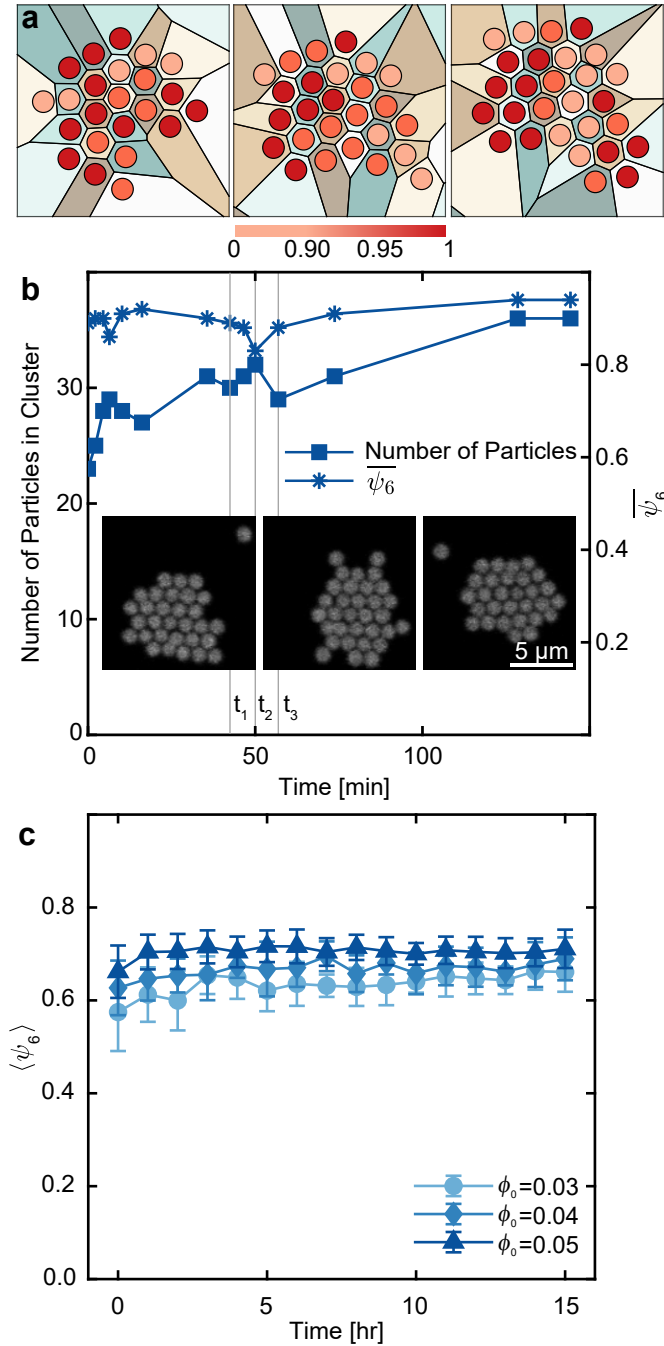
Fig. 4 The structure of the clusters during their evolution. (a) 2-D rendering of the particle positions and the corresponding Voronoi tessellation of a representative cluster from a suspension with $\phi_0 = 0.03$, 0.3 c/c^* PAM, and 30 mM NaOH. Particles are colored according to ψ_6, as indicated by the color bar below the images. (b) Number of particles in cluster (left y-axis) and $\overline{\psi}_6$ (right y-axis) as a function of time for a suspension with $\phi_0 = 0.03$, 0.3 c/c^* PAM, and 30 mM NaOH. (c) Ensemble averaged $\langle \psi_6 \rangle \sim 0.7$ as a function of time for clusters in suspensions with [PAM]= 0.3 c/c^*, [NaOH] = 30 mM, and $\phi_0 = 0.03$, 0.04, and 0.05. The error bars indicate one standard deviation from the mean.

leading to a greater number of smaller clusters. As the monomer volume fraction ϕ_m decreases from ϕ_0 towards ϕ_e (Fig. 3(c)), the nucleation rate drops. Since nucleation requires a certain threshold supersaturation, i.e., excess of monomers over their equilibrium volume fraction ϕ_e, one would expect that after ϕ_m steadies at ϕ_e no new clusters would nucleate and the number of clusters would remain steady. The decreasing number of clusters deviates from this expectation and reveals that maturation processes have started instead.

The cluster population may maturate through two mechanisms. First, the cluster may diffuse towards one another and coalesce, leading to larger new clusters. Coalescence is expected to dominate cluster maturation at the long times necessary for the relatively large clusters to diffuse towards one another.[70] A different mechanism, often referred to as Ostwald ripening, is expected to dominate at shorter times after nucleation ceases.[71,72] Ostwald ripening is driven by the excess free energy of smaller clusters: a greater relative number of the particles locate at the periphery, where they bond to fewer neighbors than the particles in the cluster bulk.[73,74] This excess free energy makes the particle suspension undersaturated with respect to small clusters as ϕ_m approaches ϕ_e and they dissolve, releasing monomers. The monomers diffuse towards larger clusters, with respect to which the suspension is supersaturated because they hold a lower number of periphery particles. Mathematical models of the kinetics of Ostwald ripening predict that the average cluster size increases as $t^{1/3}$ if the rate of particle exchange is governed by diffusion between the clusters (this subcase is referred to as diffusion control) and as $t^{1/2}$ if particle association to the large clusters represents the rate-limiting step (kinetic control).[75,76]

To distinguish between the two mechanisms of maturation, we examine the kinetics of cluster growth on long time scales. At times longer than ≈ 3.5 h, at which the number of clusters is at a maximum and cluster maturation begins (Fig. 5(a)), the average number of particles in a cluster N increases as a power law with time,

$$N = at^b, \qquad (3)$$

where a and b are free parameters (Fig. 6(a)). Power-law fits to the long-time growth curves in Fig. 6a yield exponents of 0.72 ± 0.01, 0.54 ± 0.01, and 0.57 ± 0.02 for initial volume fractions $\phi_0 = 0.03$, 0.04 and 0.05, respectively.

The models of maturation use the average cluster radius as their main variable, whereas we characterize the cluster size as the number N of particles in a cluster. The average number of particles in a cluster N scales with the average cluster radius of gyration $R_{g,c}$ via the average fractal dimension d_f of the clusters,

$$R_{g,c} = CN^{1/d_f}, \qquad (4)$$

where the size constant $C = 0.6$ μm is comparable to the hydrodynamic radius of our particles. At the three tested volume fractions, the values of d_f obtained from power-law fits are nearly constant (Fig. 6(b)); at 15 h, $d_f = 1.795 \pm 0.002$, 1.882 ± 0.002, and 1.792 ± 0.010 for suspensions with $\phi_0 = 0.03$, 0.04, and 0.05, respectively (Fig. 6(c)). We conclude that d_f is constant in time throughout cluster evolution, similar to the order parameter ψ_6

and consistent with expectations for classical nucleation of clusters. Importantly for the identification of the maturation mechanism, all three values of d_f are close to 2, the value for compact isometric two-dimensional clusters.

Fig. 6 Determination of the mechanism of cluster maturation. (a) Average cluster size as a function of time. The straight lines indicate power-law fits and the numbers indicate the corresponding power-law exponents. (b) Cluster radius of gyration $R_{g,c}$ as a function of the number of particles in the cluster, N, at 15 hours. Red line: curve fit of equation (4) with ϕ_0 = 0.03 (circle). (c) Average fractal dimension d_f as a function of time. All samples are suspensions with [PAM] = $0.3c/c^*$, [NaOH] = 30 mM, and initial volume fractions ϕ_0 = 0.03 (circle), 0.04 (diamond) and 0.05 (triangle).

Using the measured d_f values, we combine eqns. 3 and 4 to obtain the scaling of cluster size with time as

$$R_{g,c} = aCt^{b/d_f}. \qquad (5)$$

In our experiments, we find that $R_{g,c}$ grows with time as a power law with exponents of 0.40±0.01, 0.29±0.01, and 0.32±0.01 for initial volume fractions ϕ_0 = 0.03, 0.04 and 0.05, respectively. These exponents are close to the value of 1/3 expected for Ostwald ripening under diffusion-limited conditions.[75,76] The exponent characterizing the growth of clusters over time does not increase at longer times (Fig. 6(c)). This observation suggests that we do not observe coalescence on these time scales, which would be indicated by a transition to a larger scaling exponent on long
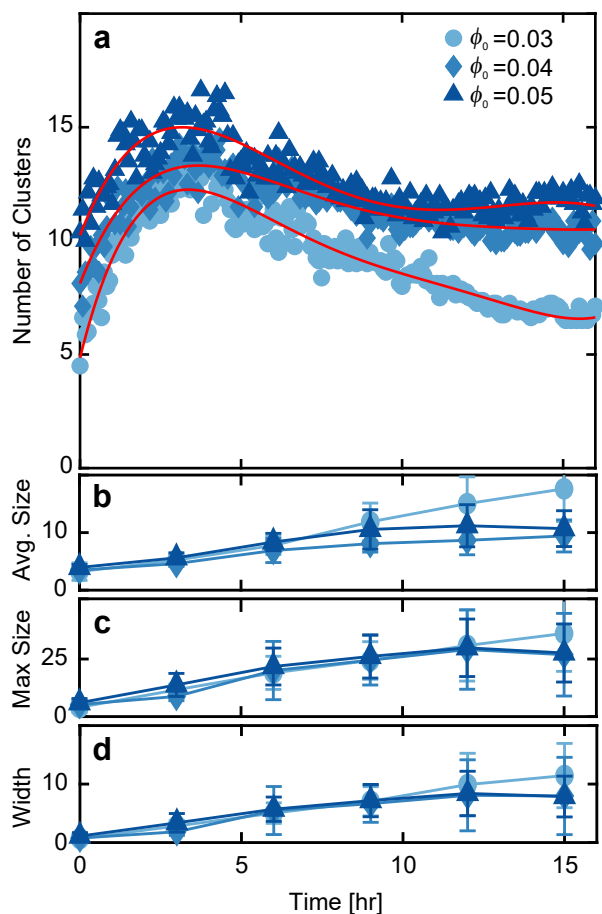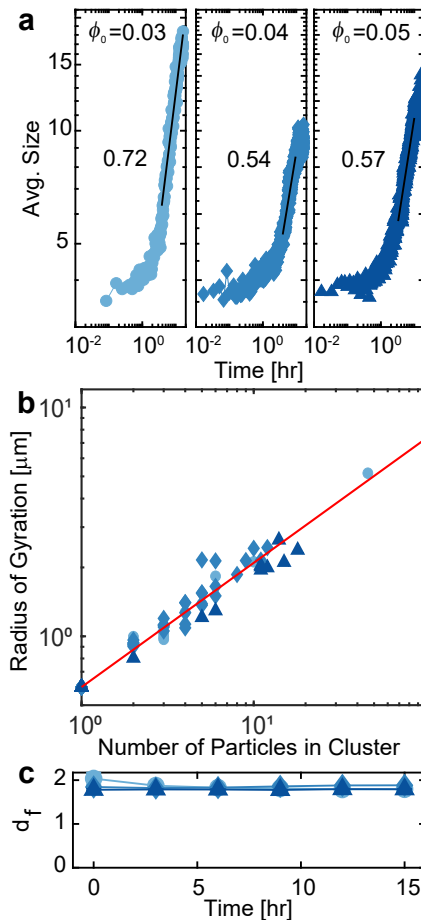

Fig. 5 Time evolution of clusters. (a) Total number of clusters, the (b) average and (c) maximum cluster size, and (d) the width of the cluster size distribution as a function of time for three initial particle volume fractions ([PAM]= 0.3 c/c^* and [NaOH] = 30 mM). The red curves in (a) are fourth-order polynomial fits and are a guide to the eye. The error bars indicate one standard deviation from the mean.

times.[70] This transition would be governed by the characteristic time for clusters to diffuse over the distances that separate them. The relatively large cluster sizes impede their diffusion and move coalescence to times longer than 15 hours that we probe in these experiments.

4 Conclusions

We develop a colloidal system with tunable interactions to investigate the nucleation and growth of colloid crystals from dilute suspensions. We find that the studied colloidal system adequately models the nucleation and maturation of crystal populations of small-molecule solutes. The top and bottom walls of the observation chamber constrain particle motions to two dimensions, in which the particles retain fully diffusive behavior with only moderately impeded diffusion coefficient. The particles form two-dimensional clusters with nearly perfect hexagonal structure. At long times, equilibrium sets in between particles in the suspension and those in the clusters. The volume fraction of the suspension in equilibrium, the particle solubility, can be predicted from the depth of the interparticle attraction at low and moderate electrolyte concentrations. Clusters structure as hexagonal two-dimensional crystals independent of their size, age, and time of formation as well as the suspension initial volume fraction, indicating that the clusters nucleate classically, directly in the suspension, and cluster nucleation is not hosted and assisted by distinctly structured precursor, as envisioned in nonclassical nucleation scenarios. After nucleation ceases owing to depleted supersaturation, the number of clusters drops and the average cluster radius grows approximately with the cubic root of time, indicating that the cluster population maturates primarily through Ostwald ripening, controlled by slow particle diffusion from small to large clusters. We anticipate that this model system can be used to explore how interparticle interactions affect the pathways of crystallization from solution.

5 Acknowledgements

Notes and references

1 National Research Council, *Frontiers in Crystalline Matter: From Discovery to Technology*, The National Academies Press, Washington, DC, 2009.

2 J. J. De Yoreo, A. K. Burnham and P. K. Whitman, *Int. Mater. Rev.*, 2002, **47**, 113–152.

3 J. W. Gibbs, *The Scientific Papers of J. Willard Gibbs, Vol. 1: Thermodynamics*, Oxbow Press, 1993.

4 J. W. Gibbs, *Trans. Conn. Acad.*, 1878, **3**, 343–524.

5 J. W. Gibbs, *Trans. Conn. Acad.*, 1876, **3**, 108–248.

6 L. Farkas, *Z. Phys. Chem.*, 1927, **125U**, 236–242.

7 M. Volmer and W. Schultze, *Z. Phys. Chem.*, 1931, **156A**, 1–22.

8 M. Volmer, *Kinetik der Phasenbildung*, Steinkopff, 1939.

9 R. Becker and W. Döring, *Ann. Phys. (Berl.)*, 1935, **416**, 719–752.

10 Y. B. Zeldovich, *Acta Physicochim. U.R.S.S.*, 1943, **18**, 1.

11 W. K. Burton, N. Cabrera, F. C. Frank and N. F. Mott, *Philos. Trans. Royal Soc. A*, 1951, **243**, 299–358.

12 A. A. Chernov, *Phys. Usp.*, 1961, **4**, 116–148.

13 M. A. Kaissaratos, *PhD thesis*, University of Houston, 2016.

14 M. D. Oleksiak, J. A. Soltis, M. T. Conato, R. L. Penn and J. D. Rimer, *Chem. Mater.*, 2016, **28**, 4906–4916.

15 T. Yamazaki, Y. Kimura, P. G. Vekilov, E. Furukawa, M. Shirai, H. Matsumoto, A. E. S. V. Driessche and K. Tsukamoto, *Proc. Natl. Acad. Sci. USA*, 2017, **114**, 2154–2159.

16 J. De Yoreo, in *A Perspective on Multistep Pathways of Nucleation*, American Chemical Society, 2020, ch. 1, pp. 1–17.

17 P. G. Vekilov, in *Nonclassical Nucleation*, American Chemical Society, 2020, ch. 2, pp. 19–46.

18 S. Jeon, T. Heo, S.-Y. Hwang, J. Ciston, K. C. Bustillo, B. W. Reed, J. Ham, S. Kang, S. Kim, J. Lim, K. Lim, J. S. Kim, M.-H. Kang, R. S. Bloom, S. Hong, K. Kim, A. Zettl, W. Y. Kim, P. Ercius, J. Park and W. C. Lee, *Science*, 2021, **371**, 498–503.

19 A. E. S. Van Driessche, N. Van Gerven, R. R. M. Joosten, W. L. Ling, M. Bacia, N. Sommerdijk and M. Sleutel, *Nat. Commun.*, 2021, **12**, 3902.

20 M. W. Anderson, M. Bennett, R. Cedeno, H. Cölfen, S. J. Cox, A. J. Cruz-Cabeza, J. J. De Yoreo, R. Drummond-Brydson, M. K. Dudek, K. A. Fichthorn, A. R. Finney, I. Ford, J. M. Galloway, D. Gebauer, R. Grossier, J. H. Harding, A. Hare, D. Horváth, L. Hunter, J. Kim, Y. Kimura, C. E. A. Kirschhock, A. A. Kiselev, W. Kras, C. Kuttner, A. Y. Lee, Z. Liao, L. Maini, S. O. Nilsson Lill, N. Pellens, S. L. Price, I. B. Rietveld, J. D. Rimer, K. J. Roberts, J. Rogal, M. Salvalaglio, I. Sandei, G. Schuszter, J. Sefcik, W. Sun, J. H. ter Horst, M. Ukrainczyk, A. E. S. Van Driessche, S. Veesler, P. G. Vekilov, V. Verma, T. Whale, H. P. Wheatcroft and J. Zeglinski, *Faraday Discuss.*, 2022, **235**, 219–272.

21 M. Sleutel, J. Lutsko, A. E. Van Driessche, M. A. Durán-Olivencia and D. Maes, *Nat. Commun.*, 2014, **5**, 5598.

22 A. E. S. Van Driessche, N. Van Gerven, P. H. H. Bomans, R. R. M. Joosten, H. Friedrich, D. Gil-Carton, N. A. J. M. Sommerdijk and M. Sleutel, *Nature*, 2018, **556**, 89–94.

23 H. H. Teng, P. M. Dove, C. A. Orme and J. J. de Yoreo, *Science*, 1998, **282**, 724–727.

24 L. M. Hamm, A. J. Giuffre, N. Han, J. Tao, D. Wang, J. J. D. Yoreo and P. M. Dove, *Proc. Natl. Acad. Sci. USA*, 2014, **111**, 1304–1309.

25 S. Whitelam, *Phys. Rev. Lett.*, 2010, **105**, 088102.

26 S.-T. Yau and P. G. Vekilov, *Nature*, 2000, **406**, 494–497.

27 R. A. W. Pu S., Gong C., *R. Soc. Open Sci.*, 2020, **7**, 191204.

28 S. Chung, S.-H. Shin, C. R. Bertozzi and J. J. De Yoreo, *Proc. Natl. Acad. Sci. USA*, 2010, **107**, 16536—16541.

29 A. McPherson, Y. Kuznetsov, A. Malkin and M. Plomp, *J. Struct. Biol.*, 2003, **142**, 32–46.

30 S.-T. Yau and P. G. Vekilov, *J. Am. Chem. Soc.*, 2001, **123**,

1080–1089.

31 N. D. Loh, S. Sen, M. Bosman, S. F. Tan, J. Zhong, C. A. Nijhuis, P. Král, P. Matsudaira and U. Mirsaidov, *Nat. Chem.*, 2017, **9**, 77–82.

32 Z. Ou, Z. Wang, B. Luo, E. Luitjen and Q. Chen, *Nat. Mater.*, 2020, **19**, 450– 455.

33 Y. Zhong, V. R. Allen, J. Chen, Y. Wang and X. Ye, *J. Am. Chem. Soc.*, 2022, **144**, 14915–14922.

34 Z. Wang, C. Liu and Q. Chen, *J. Cryst. Growth*, 2023, **601**, 126955.

35 J. Smith and Q. Chen, *Microsc. Microanal.*, 2021, **27**, 1314–1315.

36 U. Mirsaidov, J. P. Patterson and H. Zheng, *MRS Bull.*, 2020, **45**, 704–712.

37 R. Egerton, P. Li and M. Malac, *Micron*, 2004, **35**, 399–409.

38 A. Castellanos-Gomez, X. Duan, Z. Fei, H. R. Gutierrez, Y. Huang, X. Huang, J. Quereda, Q. Qian, E. Sutter and P. Sutter, *Nat. Rev. Methods Primers*, 2022, **2**, 58.

39 X. Zhang, Y. He, M. L. Sushko, J. Liu, L. Luo, J. J. D. Yoreo, S. X. Mao, C. Wang and K. M. Rosso, *Science*, 2017, **356**, 434–437.

40 S. Auer, W. C. K. Poon and D. Frenkel, *Phys. Rev. E Stat. Nonlin. Soft Matter Phys.*, 2003, **67 2 Pt 1**, 020401.

41 U. Gasser, *J. Phys.: Condens. Matter*, 2009, **21**, 203101.

42 T. Palberg, *J. Phys.: Condens. Matter*, 2014, **26**, 333101.

43 K. Kratzer and A. Arnold, *Soft Matter*, 2015, **11**, 2174–2182.

44 A. Murakado, A. Toyotama, M. Yamamoto, R. Nagano, T. Okuzono and J. Yamanaka, *J. Colloid Interface Sci.*, 2016, **465**, 200–207.

45 S. Guo, J. Nozawa, S. Hu, H. Koizumi, J. Okada and S. Uda, *Langmuir*, 2017, **33**, 10543–10549.

46 X. Ji, Z. Sun, W. Ouyang and S. Xu, *J. Chem. Phys.*, 2018, **148**, 174904.

47 Y. Sato, A. Toyotama, T. Okuzono and J. Yamanaka, *Chem. Lett.*, 2019, **48**, 1319–1321.

48 N. Kleppmann, F. Schreiber and S. H. L. Klapp, *Phys. Rev. E*, 2017, **95**, 020801.

49 C. Liu, Z. Ou, F. Guo, B. Luo, W. Chen, L. Qi and Q. Chen, *J. Am. Chem. Soc.*, 2020, **142**, 11669–11673.

50 W. Poon, *Science*, 2004, **304**, 830–831.

51 R. Ganapathy, M. R. Buckley, S. J. Gerbode and I. Cohen, *Science*, 2010, **327**, 445–448.

52 V. Prasad, D. Semwogerere and E. R. Weeks, *J. Phys.: Condens. Matter*, 2007, **19**, 113102.

53 J. C. Crocker and D. G. Grier, *J. Colloid Interface Sci.*, 1996, **179**, 298–310.

54 N. Park, E. J. Umanzor and J. C. Conrad, *Front. Phys.*, 2018, **6**, 42.

55 T. Kodger, R. Guerra and J. Sprakel, *Sci. Rep.*, 2015, **5**, 14635.

56 B. J. Frisken, *Appl. Opt.*, 2001, **40 24**, 4087–91.

57 D. C. Prieve, *Adv. Colloid Interface Sci.*, 1999, **82**, 93–125.

58 M. A. Bevan and D. C. Prieve, *J. Chem. Phys.*, 2000, **113**, 1228–1236.

59 S. H. Behrens and D. G. Grier, *Phys. Rev. E*, 2001, **64**, 050401.

60 S. Asakura and F. Oosawa, *J. Polym. Sci.*, 1958, **33**, 183–192.

61 H. Yukawa, *Proc. Phys. Math. Soc. Jpn. 3rd Series*, 1935, **17**, 48–57.

62 K. V. Tretiakov and K. W. Wojciechowski, *Phys. Status Solidi B*, 2020, **257**, 2000194.

63 E. Mani, W. Lechner, W. K. Kegel and P. G. Bolhuis, *Soft Matter*, 2014, **10**, 4479–4486.

64 K. A. Dill and S. Bromberg, *Molecular Driving Forces*, Garland Science, 2nd edn, 2011.

65 R. Li and Y. L. Xiong, *J. Food Sci.*, 2021, **86**, 78–85.

66 M. Muschol and F. Rosenberger, *J. Chem. Phys.*, 1995, **103**, 10424–10432.

67 F. Zhang, R. Roth, M. Wolf, F. Roosen-Runge, M. W. A. Skoda, R. M. J. Jacobs, M. Stzucki and F. Schreiber, *Soft Matter*, 2012, **8**, 1313–1316.

68 Y. L. Wu, D. Derks, A. van Blaaderen and A. Imhof, *Proc. Natl. Acad. Sci. USA*, 2009, **106**, 10564–10569.

69 Y. Mastai, *Advances in Crystallization Processes*, IntechOpen, Rijeka, 2012.

70 E. D. Siggia, *Phys. Rev. A*, 1979, **20**, 595–605.

71 J. S. Langer, *Rev. Mod. Phys.*, 1980, **52**, 1–28.

72 H. Zheng, R. K. Smith, Y. wook Jun, C. Kisielowski, U. Dahmen and A. P. Alivisatos, *Science*, 2009, **324**, 1309–1312.

73 W. Ostwald, *Z. Phys. Chem.*, 1897, **22U**, 289–330.

74 I. N. Stranski and R. Kaischew, *Z. Phys. Chem.*, 1937, **35B**, 427 – 432.

75 I. Lifshitz and V. Slyozov, *J. Phys. Chem. Solids*, 1961, **19**, 35–50.

76 C. Wagner, *Z. Elehtrochem., Ber. Bunsenges. Phys. Chem.*, 1961, **65**, 581–591.